Functional Pyrimidinyl Pyrazolate Pt(II) Complexes: Role of Nitrogen Atom in Tuning the Solid-State Stacking and Photophysics

Paramaguru Ganesan, Wen-Yi Hung, Jen-Yung Tso, Chang-Lun Ko, Tsai-Hui Wang, Po-Ting Chen, Hsiu-Fu Hsu,* Shih-Hung Liu, Gene-Hsiang Lee, Pi-Tai Chou,* Alex K.-Y. Jen,* and Yun Chi**

Pt(II) metal complexes are known to exhibit strong solid-state aggregation and are promising for realization of efficient emission in fabrication of organic light emitting diodes (OLED) with nondoped emitter layer. Four pyrimidine–pyrazolate based chelates, together with four isomeric Pt(II) metal complexes, namely: [Pt(pm2z)$_2$], [Pt(tpm2z)$_2$], [Pt(pm4z)$_2$], and [Pt(tpm4z)$_2$], are isolated and systematically investigated for their structure–property relationships for practical OLED applications. Detailed single molecular and aggregated structures are revealed by photophysical and mechanochromic measurements, grazing-incidence X-ray diffraction, and theoretical approaches. These results suggest that these Pt(II) emitters pack like a deck of playing cards under vacuum deposition, and their emission energy is not only affected by the single molecular designs, but notably influenced by their intermolecular packing interaction, i.e., Pt···Pt separations that are arranged in the order: [Pt(tpm4z)$_2$] > [Pt(pm4z)$_2$] > [Pt(tpm2z)$_2$] > [Pt(pm2z)$_2$]. Nondoped OLED with emission ranging from green to red are prepared, to which the best performances are recorded for [Pt(tpm2z)$_2$], giving maximum external quantum efficiency (EQE) of 27.5% at 10^3 cd m^{-2}, maximum luminance of 2.5×10^5 cd m^{-2} at 17 V, and with stable CIE$_{x,y}$ of (0.56, 0.44).

1. Introduction

Organic light emitting diodes (OLED) have been spurred by the fast advancement of modern display technologies of laptop computers, notepads, and cell phones. Their efficiencies have been improved during the past two decades using suitable third-row transition-metal phosphors as emitters. Among these emitters, Pt(II) metal complexes have been attracting intensive studies owing to their higher stability and intense luminescence at room temperature (RT).[1] However, in contrast to the Ir(III) emitters with d^6-electronic configuration and octahedral coordination structure,[2] the Pt(II) emitters possesses distinctive d^8-configuration and square planar geometry, which induced a greater tendency in forming π–π-stacking interaction between adjacent molecules in solid state. As for application, this aggregation is capable of tuning emission to lower energy region of the visible spectra and even further into the near-infrared (NIR), which allows versatile prospective in applications for this class of emitters.

Many aggregated Pt(II) complexes have been synthesized, for which their structures can be differentiated into two classes. One is best represented by those bearing a linear Pt$_n$ architecture and with Pt···Pt distance of less than 3.4 Å; the latter is the sum of van del wall radii of

---

Dr. P. Ganesan, Prof. Y. Chi
Department of Chemistry
National Tsing Hua University
Hsinchu 30013, Taiwan
E-mail: ychi@mx.nthu.edu.tw
Prof. W.-Y. Hung, J.-Y. Tso, C.-L. Ko
Institute of Optoelectronic Sciences
National Taiwan Ocean University
Keelung 202, Taiwan
E-mail: wenhung@mail.ntou.edu.tw
Dr. T.-H. Wang, P.-T. Chen, Prof. H.-F. Hsu
Department of Chemistry
Tamkang University
New Taipei 25137, Taiwan
E-mail: hhsu@mail.tku.edu.tw

Dr. S.-H. Liu, Dr. G.-H. Lee, Prof. P.-T. Chou
Department of Chemistry and Instrumentation Center
National Taiwan University
Taipei 10617, Taiwan
E-mail: chop@ntu.edu.tw
Prof. A. K.-Y. Jen, Prof. Y. Chi
Department of Materials Science and Engineering
and Department of Chemistry
City University of Hong Kong
Hong Kong SAR
E-mail: alexjen@cityu.edu.hk

The ORCID identification number(s) for the author(s) of this article can be found under https://doi.org/10.1002/adfm.201900923.

DOI: 10.1002/adfm.201900923

carbon atom, symbolized the shortest possible Pt–Pt distance without causing major distortion to the coordinative chelates. This linear-chain arrangement has been reported in several examples, such as $[Pt(NH_3)_4][PtCl_4]$ (Magnus Green Salt),[3] $[Pt(diimine)_2(CN)_2]$, diimine = bipyridine and biisoquinoline,[4] $[Pt(diBrbpy)(C{\equiv}CC_6H_4Et\text{-}4)_2]$, diBrbpy = 4,4-dibromo-2,2′-bipyridine,[5] and $[Pt(DECO)_2]_n$, DECO = cyano-2-oximino-*N*,*N*′-diethylaminoacetamide.[6] The corresponding Pt(II) units are held together by noncovalent metallophilic Pt···Pt interaction, as shown by the single crystal X-ray diffraction studies. Alternatively, there are also a second class of Pt(II) complexes that showed the reduced Pt···Pt interaction between a pair of nearby Pt(II) fragments.[7] These "dinuclear" complexes can be either physically assembled using bridging ligand(s),[8] supported via the metallophilic Pt···Pt interaction mentioned in the linear chain type of Pt(II) complexes,[9] or even forced to form the Pt(II) dimers upon addition of cucurbit[8]uril macrocycles.[10] In general, these Pt(II) complexes would exhibit bright "assembly-induced" phosphorescence, which may be either independent or sensitive to their physical conditions and external stimulation.

Concurrently, there is a growing interest in the series of Pt(II) complexes with pyrazolate-containing chelates and in studies of the photophysical effect induced by aggregation in solid states.[11] One of interesting examples is ascribed to Pt(II) complex $[Pt(fppz)_2]$, fppz = 3-(trifluoromethyl)-5-(2-pyridinyl) pyrazolate, c.f. **Scheme 1**,[11b] which possessed a columnar packing arrangement, as well as large red shift in both photoluminescence (PL) and electroluminescence (EL).[12] This complex is also known for forming highly ordered crystalline structure in vacuum deposited thin film, similar to that observed in many Pt(II) porphyrin derivatives.[13] However, the record-high emission of $[Pt(fppz)_2]$ ($\Phi \approx 96\%$) allowed the fabrication of a nondoped OLED with a remarkably high external quantum efficiency (EQE) of 31.1%.[14] Moreover, the ordered morphology in the vacuum deposited thin film has induced the horizontal arranged emitting dipole ratio of 93%, giving a very high EQE of 38.8% for orange-emitting OLED using such thin film crystalline as the emitting layer.[15]

Knowing their tendency in forming crystalline thin film, we also functionalized $[Pt(fppz)_2]$ by substituting pyridyl with pyrazinyl fragment to give $[Pt(fprpz)_2]$, in anticipation of obtaining further red-shifted emission.[16] Emission peak maximum at 740 nm, quantum yield (QY) of 81% and lifetime of 313 ns were observed; all are attributable to the metal-metal-to-ligand charge transfer (MMLCT) character in the emitting triplet excited states. The NIR-emitting OLED gave EQE of 24 ± 1% and maximum radiance of $(3.6 \pm 0.2) \times 10^5$ mW $sr^{-1}\cdot m^{-2}$ without the light out-coupling hemisphere structure; affording the highest record among NIR OLED.

In this contribution, we proceed to investigate the structure–property relationship of functional $[Pt(fprpz)_2]$ by relocating the noncoordinating N-atom in pyrazinyl fragment, forming either 2-pyrimidinyl or 4-pyrimidinyl substituted pyrazolate Pt(II) complexes, c.f. Scheme 1. Interestingly, photophysical properties such as emission peak wavelength, quantum yield and response to the physical states and external mechano-stimulus were affected not only by the location of noncoordinating N-atom but also by their substituents, i.e., R = H and ^{t}Bu. Detailed analyses conclude that the variations are mainly attributed to a change of intermolecular stacking (i.e., Pt···Pt interaction) that constituted a special case for the aggregated induced emission (AIE).[17] Moreover, fabrication of nondoped phosphorescent OLED were also conducted and discussed in the following sections.

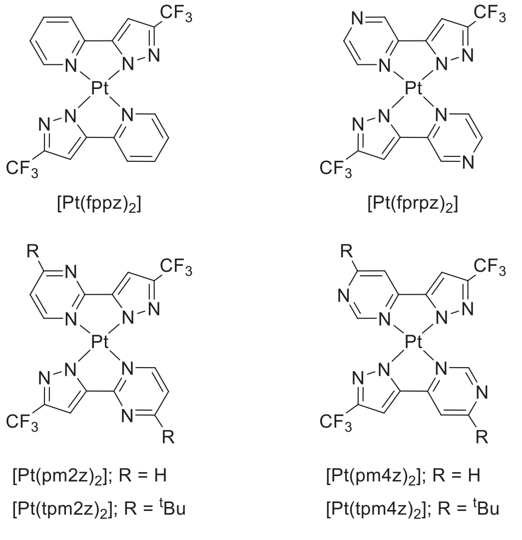

Scheme 1. Structural drawing of the studied Pt(II) complexes bearing various pyrazolate-containing chelates.

2. Results and Discussion

2.1. Syntheses and Characterization

The synthetic protocols of the pyrimidine pyrazole chelates employed in the present studies are outlined in **Schemes 2** and **3**, to which the detailed experimental procedures are elaborated in supporting information. Preparation of all four pyrimidine ligands demanded the acetyl derivatives as key intermediates. Hence, reaction of 2-pyrimidinecarbonitrile (pm-2CN) with methyl

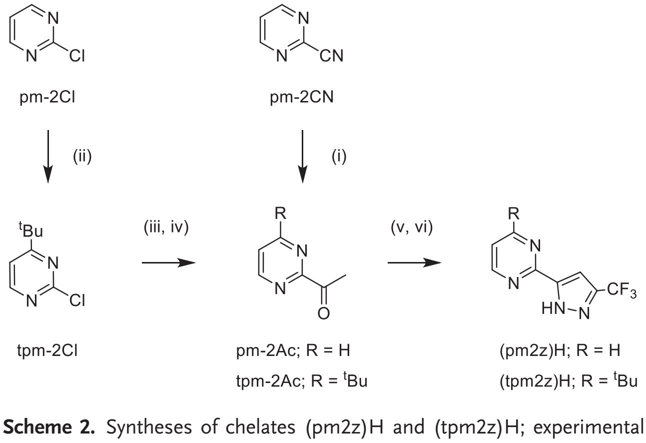

Scheme 2. Syntheses of chelates (pm2z)H and (tpm2z)H; experimental conditions: i) MeMgBr, ether, 0 °C, 4 h. ii) Pivalic acid, $K_2S_2O_8$, $AgNO_3$, H_2SO_4, iii) ethoxyethenyl-tri-*n*-butylstannane, $Pd(PPh_3)_2Cl_2$, iv) 2 N HCl, acetone, RT, v) CF_3CO_2Et, NaOEt, and vi) $N_2H_4{\cdot}H_2O$, p-TsOH, EtOH, reflux.

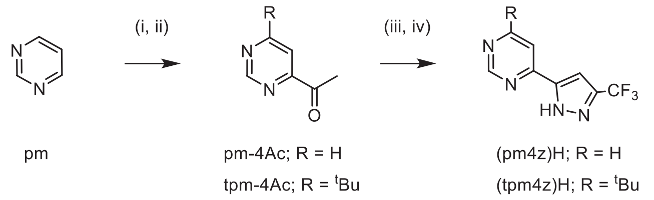

Scheme 3. Syntheses of chelates (pm4z)H and (tpm4z)H; experimental conditions: i) paraldehyde, $tBuO_2H$, CF_3CO_2H, $FeSO_4{\cdot}7H_2O$, CH_3CN, ii) pm-4Ac, pivalic acid, $K_2S_2O_8$, $AgNO_3$, H_2SO_4, iii) CF_3CO_2Et, NaOEt, and iv) $N_2H_4{\cdot}H_2O$, p-TsOH, EtOH, reflux.

magnesium bromide yielded 2-acetyl pyrimidine (pm-2Ac). Alternatively, the t-butyl analogue of pm-2Ac (i.e., tpm-2Ac) was obtained by reaction of 2-chloro pyrimidine (pm-2Cl) with pivalic acid, followed by treatment with tri-*n*-butyl-1-ethoxyvinylstannane to yield the ethoxy vinyl derivative, which could be readily hydrolyzed to form the tpm-2Ac. As for 4-substituted acetyl pyrimidine (pm-4Ac), it can be synthesized by the direct acetylation of pyrimidine with paraldehyde, while the reaction of pm-4Ac with pivalic acid, in presence of both $K_2S_2O_8$ and $AgNO_3$, results in the formation of its ^{t}Bu analogue, i.e., tpm-4Ac in good yields.

With these acetyl substituted pyrimidines in hands, we conducted the Claisen condensation with ethyl trifluoroacetate to form diketone intermediates. Subsequent cyclization with hydrazine hydrate yielded the target pyrimidinyl pyrazole chelates, c.f. (pm2z)H, (tpm2z)H, (pm4z)H, and (tpm4z)H. All corresponding Pt(II) complexes $[Pt(pm2z)_2]$, $[Pt(tpm2z)_2]$, $[Pt(pm4z)_2]$ and $[Pt(tpm4z)_2]$ were next synthesized by treatment of $[PtCl_2(DMSO)_2]$ with these pyrazole ligands with addition of Na_2CO_3 in refluxing 2-methoxyethanol. The resulting Pt(II) complexes exhibited poor solubility in 2-methoxyethanol (and other solvents as well) and were immediately precipitated out of the solution even during reflux. For workup, all precipitates were collected by filtration, washing with water and ether in sequence and, finally, were sublimed under high vacuum to produce the analytically pure samples. It is notable that all these chelates contain a trifluoromethyl (CF_3) substituent on pyrazole, giving increased electron deficiency at the Pt(II) metal center upon formation of Pt(II) complexes. Moreover, upon further consideration of its reduced van der Waals attraction and smaller size (only slightly larger than methyl group), the complexes may result in an improved intermolecular stacking. Overall, this CF_3 group is probably a key player in formation of the well-stacked (crystalline) thin film of these highly emissive Pt(II) complexes.

These Pt(II) complexes were characterized using ^1H and ^{19}F NMR spectroscopies, mass spectrometry and elemental analyses. The ^1H and ^{19}F NMR spectra were generally taken at higher temperature (80 °C) because of their poor solubility in common organic solvents such as dimethyl sulfoxide (DMSO) and toluene. However, $[Pt(pm4z)_2]$ represents one exception as it is reasonably soluble in acetone at RT. A characteristic downfield signal at δ 9.8–10.50 was observed in the ^1H NMR spectrum of all Pt(II) complexes. These unique signals were assigned to the CH unit next to the coordinated nitrogen atom of pyrimidinyl fragment, confirming the existence of interligand $C{-}H\cdots N$ bonding to the nearby pyrazolate, as observed in many related pyrazolate complexes.[18] Due to improved solubility, the crystal of $[Pt(pm4z)_2]$ was successfully grown from acetone and hexane at RT. It is notable that the red-emitting powder of $[Pt(pm4z)_2]$ turned colorless upon dissolution in acetone and, eventually, formed yellow crystals, which are green emitting, by slow addition of hexane. This variation of photophysical property is apparently due to the weakening of intermolecular π–π stacking and disruption of $Pt\cdots Pt$ interaction, upon dissolution in acetone and formation of single crystals.

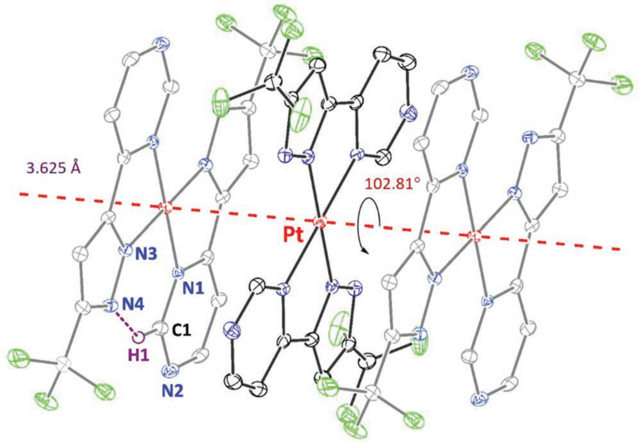

Figure 1. Structural drawing of $[Pt(pm4z)_2]$ with ellipsoids shown at the 30% probability level; selected bond distances: Pt(1)-N(1) = 2.036(3), Pt(1)-N(3) = 1.995(3) and $Pt(1)\cdots Pt(1)$ = 3.625 and $N(4)\cdots H(1)$ = 2.271 Å, and bond angles: N(1)-Pt(1)-N(3A) = 100.99(13), N(1)-Pt(1)-N(3) = 79.01(13)°.

Single crystal X-ray structural determination of $[Pt(pm4z)_2]$ was next executed. Molecules in crystal lattices constituted an infinite 1D chain-like arrangement along the *b*-axis of unit cells. However, **Figure 1** shows the packing structure involving only three molecules that are separated by an elongated $Pt\cdots Pt$ distance of ≈3.625 Å. The pm4z chelates in Pt(II) complex are arranged in the mutual *trans*-orientation, while the adjacent Pt(II) complexes are rotated around the Pt–Pt axis by 102.81°, followed by a second 77.19° (i.e., 180–102.81°) rotation to regenerate the third molecule with identical orientation, so that the pyrazolate and pyrimidine fragments of the pm4z chelate are sandwiched by their adjacent counterparts of Pt(II) complexes. Overall, this single crystal X-ray structural analysis confirmed that the observed green emission from single crystals originates from the isolated molecules, while the red-emitting, sublimed powders (or even vacuum deposited thin film) may possess a distinctive morphology with an increased $Pt\cdots Pt$ stacking interaction. Interestingly, no acetone molecule can be located on the electron density map of single crystal X-ray structural analyses, probably due to its nonexistence or in disordered arrangement.

2.2. Photophysical Properties

Figure 2 displays the UV–vis absorption and emission spectra of these Pt (II) metal complexes as vacuum deposited thin film, while the pertinent numerical data are summarized in **Table 1**. The data in solution were not reported due to their poor solubility in majority of organic solvents. For the thin film spectra, intense absorption bands appeared in the higher-energy region (<350 nm) are attributed to the ligand-centered π–π* pyrazolate

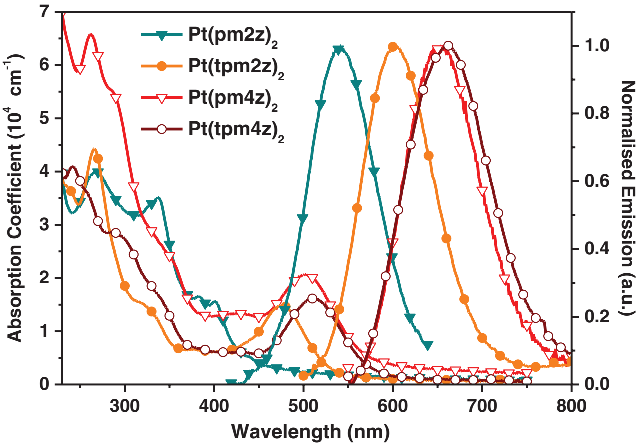

Figure 2. Absorption and emission spectra of various vacuum deposited Pt(II) thin films on quartz glass.

→ pyrimidine transitions as supported by their higher extinction coefficients. Similar transition characters and assignments are well documented in literature.[19] Their poor solubility also implicates strong aggregation which was well supported by the additional band observed around 400–512 nm arising due to the MMLCT transition.[20] In general, aggregation may induce a change from an array of isolated single Pt(II) molecule to a continuous chain-like arrangement via formation of Pt···Pt interactions. With this expectation, the lowest energy MMLCT band of [Pt(pm2z)$_2$] at 400 nm (or lack of lower energy MMLCT absorption band) may suggest a relatively diminished Pt···Pt interaction. In contrast, after introducing the t-butyl substituents in forming [Pt(tpm2z)$_2$], its MMLCT absorption clearly shifted to 474 nm, showing strengthened intermolecular Pt···Pt nonbonding interaction, despite of having bulky t-butyl substituents. This stacking induced red-shift in MMLCT absorption band is further confirmed by the occurrence of enlarged S_1 energy gap of the t-butyl substituted [Pt(tpm2z)$_2$] in DMSO in comparison to its parent complex [Pt(pm2z)$_2$], which is revealed by the time-dependent density functional theory (TDDFT) calculation discussed in theoretical section, vide infra.

Alternatively, [Pt(pm4z)$_2$] and [Pt(tpm4z)$_2$] showed the MMLCT absorption band at 501 and 512 nm, respectively, which are obviously further red shifted in comparison to their pm2z analogues [Pt(pm2z)$_2$] and [Pt(tpm2z)$_2$]. This observation is in sharp contrast to the S_0-S_1 energy gap of the isolated Pt(II) complexes in TDDFT calculation, which exhibited an energy gap difference of less than 8 nm between [Pt(pm2z)$_2$] and [Pt(pm4z)$_2$] and between t-butyl substituted [Pt(tpm2z)$_2$] and [Pt(tpm2z)$_2$]. With these information, we thus propose a qualitative order of solid-state stacking interaction within these closely related Pt(II) complexes: [Pt(tpm4z)$_2$] > [Pt(pm4z)$_2$] > [Pt(tpm2z)$_2$] > [Pt(pm2z)$_2$].

The MMLCT transition can be further confirmed by their structureless emission profile with peak maximum at 542, 603, 654, and 662 nm for [Pt(pm2z)$_2$], [Pt(tpm2z)$_2$], [Pt(pm4z)$_2$], and [Pt(tpm4z)$_2$] respectively. Furthermore, relocating the pyrazolate unit from the 2nd to 4th position of pyrimidine substantially red shifted its MMLCT emission by 112 and 59 nm from the parent and t-butyl substituted pm2z derivatives. Moreover, addition of t-butyl group to the pyrimidinyl fragment of [Pt(pm2z)$_2$] induced a red shift of 61 nm in forming [Pt(tpm2z)$_2$], while there is only a small variation in the emission maximum of 8 nm upon changing from [Pt(pm4z)$_2$] to [Pt(tpm4z)$_2$]. This observation is in agreement with existence of the already strengthened Pt···Pt interaction in [Pt(pm4z)$_2$].

Figure 3 displays various photographic images of [Pt(pm2z)$_2$] recorded in ambient and under UV irradiation as well as the emission spectra recorded using spectrophotometer. The vacuum deposited thin film gave a broadened emission profile with maximum at 542 nm. In sharp contrast, the sublimed, powdery sample appears as yellow in ambient and exhibits a sky-blue emission, and feature of vibronic progression with peak maximum at 443, 470, and 499 nm. This change in emission pattern is probably due to the improved Pt···Pt interaction that existed in the vacuum deposited thin film versus the sublimed powder, for which the change of Pt···Pt interaction in powder can be verified by applying the mechanical stimulus to the sublimed powder in giving the ground powder. As can be seen, its yellow emission with maximum at 565 nm is further red-shifted versus the vacuum deposited thin film, reflecting formation of the strongest Pt···Pt interaction in the ground powder. Similar modulation of luminescent properties by aggregation of Pt(II) complexes has also been documented.[9g,21] In general, thin film deposition demands a slow transfer of vaporized molecule onto the cold substrate surface, while sublimation involves a fast transport of larger quantity of samples, to which the vacuum deposition and sublimation are under thermodynamic and kinetic control respectively, causing substantial difference in intermolecular packing interaction.

Alternatively, both vacuum deposited thin film and sublimed powder of third Pt(II) complex [Pt(pm4z)$_2$] exhibit relatively stronger Pt···Pt interaction, which are evidenced by their identical, red-orange emission. However, the sublimed red powder turned yellow upon dissolving in acetone, followed by reprecipitation or evaporation of solvent, and the resulted solid sample exhibits a greenish-blue emission under UV (**Figure 4**). Concomitant with this notable change in morphology, its

Table 1. Photophysical properties of Pt(II) complexes as sublimed fine powder and deposited thin film.

	Abs λ_{max} [$\varepsilon \times 10^{-4}$, M^{-1} cm^{-1}]$^{a)}$	PL λ_{max} [nm]$^{b)}$	Φ [%]$^{b)}$	τ_{obs} [ns]$^{b)}$	FWHM [cm^{-1}]
[Pt(pm2z)$_2$]	267 (4.01), 400 (1.56)	(443, 470, 499); [542]	(25); [75]	(563); [486]	(2699); [2993]
[Pt(tpm2z)$_2$]	266 (4.43), 474 (1.49)	(589); [603]	(77); [86]	(86); [327]	(2230); [2599]
[Pt(pm4z)$_2$]	262 (6.58), 501 (2.06)	(636); [654]	(52); [78]	(201); [273]	(2278); [2337]
[Pt(tpm4z)$_2$]	241 (4.09), 512 (1.62)	(648); [662]	(41); [61]	(149); [240]	(3080); [2492]

$^{a)}$UV–vis spectra were recorded using vacuum deposited thin film on quartz glass; $^{b)}$PL data measured as sublimed powder and vacuum deposited thin film at RT are depicted in parentheses and square bracket, respectively.

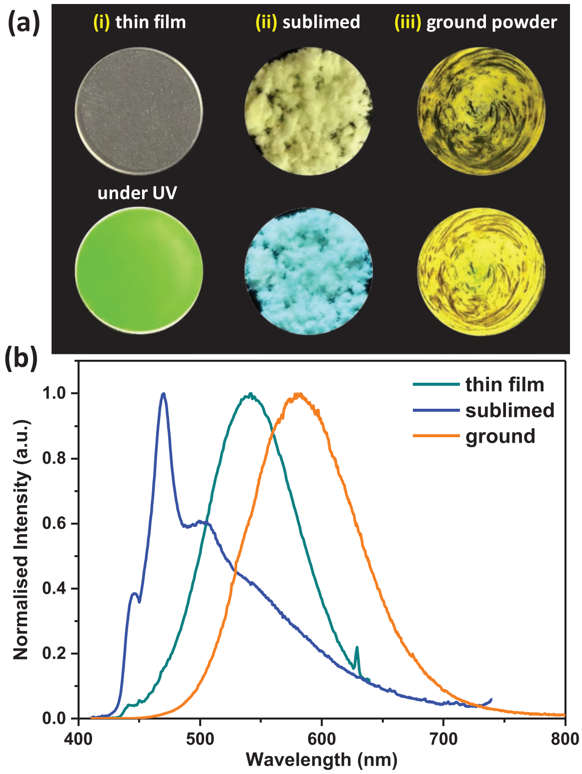

Figure 3. a) Photographs in various states of [Pt(pm2z)$_2$]: i) vacuum deposited thin film; ii) sublimed powder; iii) ground powder, taken under ambient and UV excitation at λ_{max} = 365 nm). b) Photoluminescence of [Pt(pm2z)$_2$] as deposited thin film (cyan), sublimed powder (blue), and ground powder (orange).

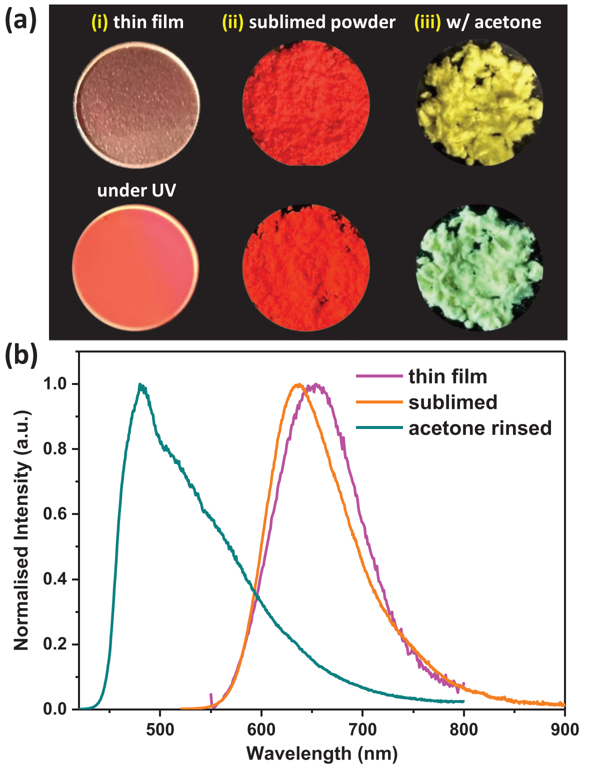

Figure 4. a) Photographs in various states of [Pt(pm4z)$_2$]: i) vacuum deposited thin film; ii) sublimed powder; iii) after acetone rinse, taken under ambient and UV excitation at λ_{max} = 365 nm. b) Photoluminescence of [Pt(pm4z)$_2$] as deposited thin film (magenta), sublimed powder (orange), and after acetone rinse (cyan).

emission maximum is now shifted from 636 to 480 nm, together with the occurrence of a less intense shoulder at 501 nm, which is attributed to the disruption of π–π stacking and weakening of Pt···Pt contact. Change of emission can be similarly achieved upon exposing to solvents such as THF, ethyl acetate, and dimethylformamide (DMF). Furthermore, [Pt(pm4z)$_2$] exhibits relatively poor solubility in acetonitrile and toluene and, hence, they did not afford a prompt change in emission, but required a much longer induction period (i.e., ≈4 h). In sharp contrast, disruption of Pt···Pt stacking was not observed upon exposure to CH_2Cl_2 or methanol even for a long period of time and at higher temperature. This solvatochromic effect is fully reversible, as the yellow powder can be reverted back to its red form upon applying mechanical stress or subjected to vacuum sublimation.

Interestingly, these morphological changes in response to solvent and mechanical stimulus are relatively less notable in their t-butyl substituted congeners [Pt(tpm2z)$_2$] and [Pt(tpm4z)$_2$]. This may be related to the notable enhancement of Pt···Pt stacking interaction upon introduction of t-butyl groups. Photographs of these samples and emission profiles are depicted in Figures S1 and S2 in the Supporting Information.

2.3. Solid-State Packing

All these Pt(II) complexes were subject to studies using synchrotron radiation facility, to which the vacuum deposited thin films of [Pt(pm2z)$_2$] and [Pt(pm4z)$_2$] showed single-crystal-like grazing-incidence X-ray diffraction (GIXD) patterns, while those of *t*-butyl derivatives [Pt(tpm2z)$_2$] and [Pt(tpm4z)$_2$] exhibited less ordered, semicrystalline patterns (Figure S3, Supporting Information). Their lattice parameters are listed in **Table 2**. Several remarks can be delineated from the recorded data. First, these thin films crystalized in the monoclinic system ($a \neq b \neq c$, $\alpha = \gamma = 90°$) with β, i.e., tilting angle of *a*-axis versus *bc* plane, being 107°, 97°, 97°, and 97° for [Pt(pm2z)$_2$], [Pt(tpm2z)$_2$], [Pt(pm4z)$_2$], and [Pt(tpm4z)$_2$], respectively. Moreover, the *b*-axis and β-angle of [Pt(pm2z)$_2$] are significantly different from other Pt(II) complexes, exhibiting a distinctive packing orientation.

Next, their electron density maps (EDMs) were derived from the 2D GIXD patterns,[22] which can be utilized to decipher and confirm their packing orientations in crystallites. **Figure 5** shows electron density maps of all studied Pt(II) complexes along the *ab* and *ac* planes, to which the tilting of molecular planes versus the substrate surface is revealed by the side views along the *ac* plane. As can be seen in their packing illustrations, the *bc* planes are tilted 19° for [Pt(pm2z)$_2$] and 7° for Pt(II) complexes [Pt(tpm2z)$_2$], [Pt(pm4z)$_2$], and [Pt(tpm4z)$_2$], which exhibit similar packing along their *ab* plane, i.e., adjacent Pt(II) molecules are offset by one-half of unit cell along the *a* axis. On the other hand, [Pt(pm2z)$_2$] showed a different in-plane packing, to which the molecules are packed on top of each other along the *a* axis. This feature can be also visualized from the *ac* plane of electron density map.

Table 2. Crystallographic data of vacuum deposited Pt(II) thin films.

	$[Pt(pm2z)_2]$	$[Pt(tpm2z)_2]$	$[Pt(pm4z)_2]$	$[Pt(tpm4z)_2]$
a [Å]	22.2	25.9	24.2	26.1
b [Å]	20.6	15.2	11.2	15.6
c [Å]	7.1	6.6	7.4	6.6
α [°]	90	90	90	90
β [°]	109	97	97	97
γ [°]	90	90	90	90
Pt···Pt [nm]	0.41	0.33	0.37	0.33
π–π [nm]	0.33	0.33	0.34	0.33
Grain size along [200] [nm]	33.4	23.8	49.1	18.1
Grain size along [020] [nm]	9.4	7.4	5.9	5.8
Grain size along [002] [nm]	8.0	4.2	6.5	3.8
Packed molecules along [100]	31	19	42	15
Packed molecules along [010]	10	6	6	8
Packed molecules along [001]	24	14	18	12
Tilting angle of molecule to the substrate normal [°]	17	0	16	0

Moreover, for both $[Pt(pm2z)_2]$ and $[Pt(pm4z)_2]$, molecular planes are tilted at 17° and 16° against substrate normal, while their t-butyl counterparts $[Pt(tpm2z)_2]$ and $[Pt(tpm4z)_2]$ aligned in a parallel manner with respect to the substrate normal. Since all samples showed similar π–π distance of 0.33 nm between the adjacent plane of stacked molecules, the enlarged tilting angle of $[Pt(pm2z)_2]$ and $[Pt(pm4z)_2]$ will produce a larger Pt···Pt separation of 0.41 and 0.37 nm in comparison to 0.33 nm that was observed for both t-butyl substituted $[Pt(tpm2z)_2]$ and $[Pt(tpm4z)_2]$. Hence, combining the influence of both the tilting angles of *c* axis and molecular plane versus substrate normal, their stacking overlap (or Pt···Pt distance) follows an order of $[Pt(tpm2z)_2] \approx [Pt(tpm4z)_2] >> [Pt(pm4z)_2] > [Pt(pm2z)_2]$. With this understanding, increase of MMLCT interaction in thin film of $[Pt(pm4z)_2]$ versus $[Pt(pm2z)_2]$, and in the t-butyl substituted derivatives $[Pt(tpm2z)_2]/[Pt(tpm4z)_2]$ versus parent complexes $[Pt(pm2z)_2]/[Pt(pm4z)_2]$ can be expected.

Finally, the grain sizes along each axis and the numbers of packed molecules within crystallite are also calculated using Scherrer equation[23] and pertinent data are listed in Table 2. The numbers of packed molecules along stacking axis [*002*] for $[Pt(pm2z)_2]$ are considerably larger than all other Pt(II) complexes, showing the largest solid-state stacking interaction among all derivatives.

2.4. Theoretical Investigation

We then executed the TDDFT calculation to gain further insights into the photophysical fundamental. However, due to the poor solubility in all common organic solvents, we choose DMSO, which is the solvent employed in majority of our NMR measurement, in constructing our simulated model. For monomer, the calculated optical and emission transition characters of all Pt(II) complexes are listed in **Table 3** and Tables S2–S5 (Supporting Information). In addition, the frontier molecular orbitals involved in the lower-lying transitions are depicted in **Figure 6** and Figures S4–S7 in the Supporting Information. The calculated $S_0 \rightarrow S_1$ optical transition are recorded to be: $[Pt(pm2z)_2]$: 370.6 nm, $[Pt(tpm2z)_2]$: 358.6 nm, $[Pt(pm4z)_2]$: 378.6 nm, and $[Pt(tpm4z)_2]$: 365.1 nm. Moreover, after geometry optimization of the T_1 excited state, the calculated $T_1 \rightarrow S_0$ emission transitions turned to $[Pt(pm2z)_2]$: 531.6 nm, $[Pt(tpm2z)_2]$: 517.5 nm, $[Pt(pm4z)_2]$: 495.9 nm, and $[Pt(tpm4z)_2]$: 486 nm. Furthermore, the $S_0 \rightarrow S_1$ transition is mainly derived from the highest occupied molecular orbital (HOMO) → lowest unoccupied molecular orbital (LUMO) transition (>97%), while the $T_1 \rightarrow S_0$ transition possesses a reduced contribution form the LUMO → HOMO process (<56%). For both S_0 and T_1 states of these Pt(II) complexes, the electron density distributions of HOMO are mainly localized at the central Pt(II) atom (≈36%) and the pyrazolates, while the electron density distributions of LUMO are mainly delocalized in the pyrimidinyl fragments and with minor contribution from the Pt(II) atom (≈5%). As a result, both the $S_0 \rightarrow S_1$ optical absorption and $T_1 \rightarrow S_0$ emission of these Pt(II) complexes in monomer are assigned to metal-to-ligand charge transfer transition (MLCT) in ≈22–18% contributions, together with ligand-to-ligand charge transfer (LLCT) and intraligand charge transfer (ILCT) transition processes.

We also perform the calculation on S_1 and T_1 of both the dimeric and trimeric stacking array. In this approach, the geometry of dimer and trimer is taken originally from truncation of the single crystal structural data of $[Pt(pm4z)_2]$ (Figure 1), followed by full structure optimization in the excited state. The obtained transition characters are listed in **Table 4** and Tables S6–S7 in the Supporting Information, while the frontier molecular orbitals involved in the lower-lying transitions are depicted in **Figure 7** and Figures S8–S9 in the Supporting Information. The calculated Pt···Pt distance is 4.40 Å in dimer and 4.05 Å in trimer. This value is a little far from the experimentally observed Pt···Pt distance 3.625 Å. This is not surprising in absence of the constraint of lattice energy, as two individual monomers would feel the repulsive force from each other and hence attempt to locate a stable geometric configuration in the global minimum with a longer Pt···Pt distance 4.40 Å. As for the trimeric structure, the middle monomer senses the repulsive forces in the opposite direction by the two neighboring monomers, forming a squeezed sandwich structure with a Pt···Pt distance (4.05 Å) shorter than that of the dimer (4.40 Å). Based on this trend, it is expected that increasing linearly aligned Pt(II) complexes, similar to the exertion of the lattice energy, should further shorten the Pt···Pt distance close to that in crystal structure.

The calculated $S_1 \rightarrow S_0$ and $T_1 \rightarrow S_0$ transitions for dimer and trimer are recorded to be 429.5 and 497.2 nm, and 435.5 and 510.2 nm, which are lowered in energy compared to those of their monomeric counterpart. For their S_1 and T_1 excited states, the electron density distributions of HOMO are mainly localized at the Pt(II) atoms (31–37% in total) and adjacent pyrazolate fragments, while the electron density distributions of LUMO are delocalized over the pyrimidinyl fragments and with less contribution from Pt(II) atoms (4.2–5.8% in total). As a result, the $S_1 \rightarrow S_0$ and $T_1 \rightarrow S_0$ transitions are

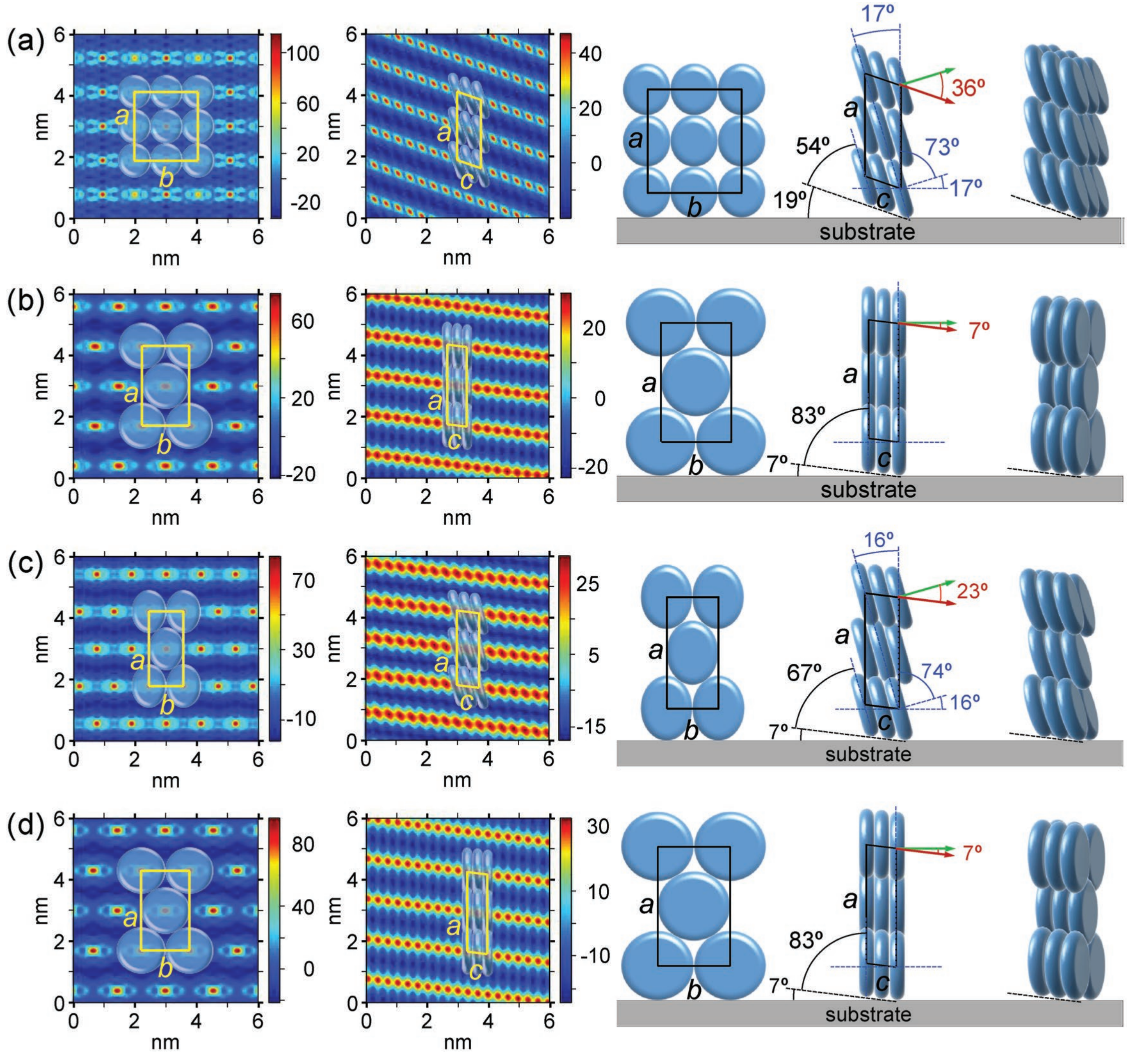

Figure 5. From left to right: EDMs along *ab* plane, *ac* plane (middle), molecular packing illustrations along *ab*, *ac* planes and perspective views of a) [Pt(pm2z)$_2$], b) [Pt(tpm2z)$_2$], c) [Pt(pm4z)$_2$], and d) [Pt(tpm4z)$_2$]. Green arrow: direction of π–π interaction, red arrow: direction of Pt···Pt interaction.

Table 3. The calculated wavelengths, transition probabilities, and main charge characters of the lowest optical absorption and emission transitions for the Pt(II) complexes [Pt(pm2z)$_2$], [Pt(tpm2z)$_2$], [Pt(pm4z)$_2$], and [Pt(tpm4z)$_2$] in DMSO.

Complex	State	λ [nm]	f	Main Assignments	MLCT
[Pt(pm2z)$_2$]	$S_0 \rightarrow T_1$	421.1	0	HOMO → LUMO (46%)	15.99%
	$S_0 \rightarrow S_1$	370.6	0.0354	HOMO → LUMO (98%)	30.14%
	$T_1 \rightarrow S_0$	531.6	0	LUMO → HOMO (50%)	17.50%
[Pt(tpm2z)$_2$]	$S_0 \rightarrow T_1$	409.1	0	HOMO → LUMO (43%)	15.78%
	$S_0 \rightarrow S_1$	358.6	0.0387	HOMO → LUMO (98%)	30.01%
	$T_1 \rightarrow S_0$	517.5	0	LUMO → HOMO (52%)	14.53%
[Pt(pm4z)$_2$]	$S_0 \rightarrow T_1$	421.7	0	HOMO → LUMO (66%)	21.56%
	$S_0 \rightarrow S_1$	378.6	0.0674	HOMO → LUMO (97%)	30.85%
	$T_1 \rightarrow S_0$	495.9	0	LUMO → HOMO (56%)	17.46%
[Pt(tpm4z)$_2$]	$S_0 \rightarrow T_1$	407.2	0	HOMO → LUMO (60%)	19.09%
	$S_0 \rightarrow S_1$	365.1	0.0955	HOMO → LUMO (97%)	30.23%
	$T_1 \rightarrow S_0$	486	0	LUMO → HOMO (52%)	15.45%

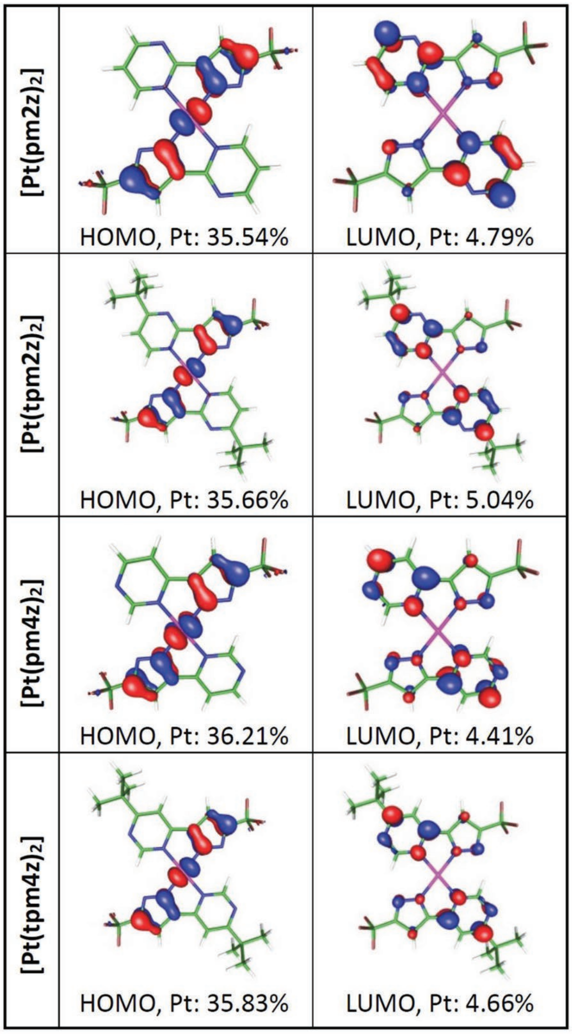

Figure 6. Frontier molecular orbital HOMO and LUMO of the ground state S_0 for all studied Pt(II) complexes. “Pt” indicates the relative electron density distribution at the Pt atoms.

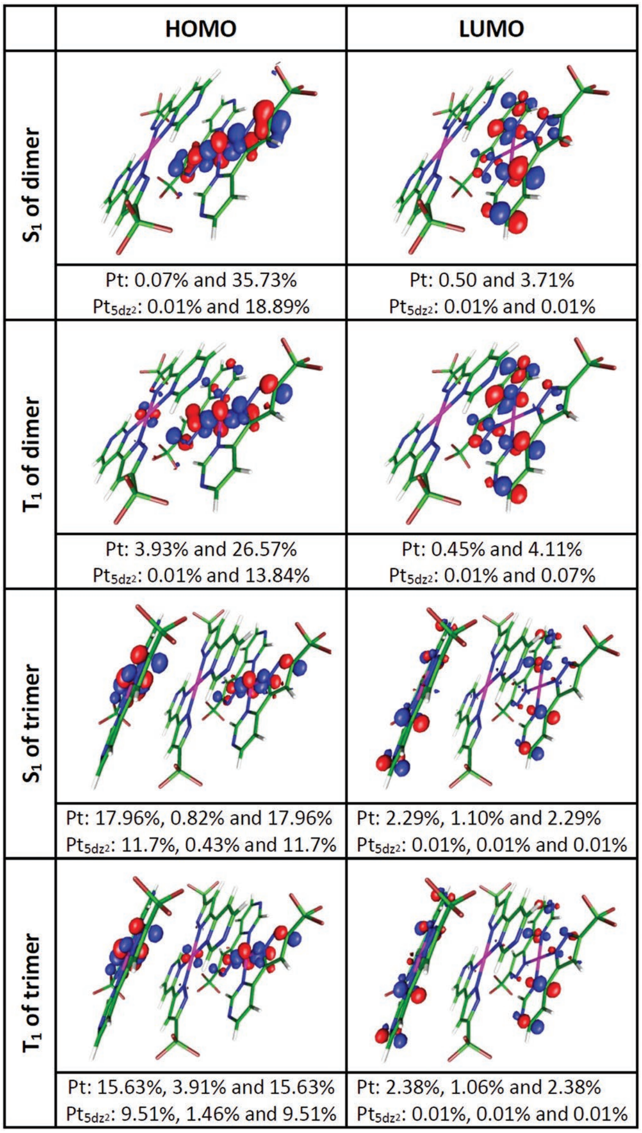

Figure 7. Frontier molecular orbital HOMO and LUMO of the excited state T_1 and S_1 for the Pt(II) complexes [Pt(pm4z)$_2$] dimer and trimer. “Pt” and “Pt$_{5dz2}$” indicate the relative electron density distribution at each Pt atom.

mainly assigned to MMLCT (≈30% for S_1 and ≈16% for T_1, respectively) mixed with certain LLCT and ILCT characters. The MMLCT transition would exert the heavy atom effect in enhancing the spin–orbit coupling that, in turn, induces the fast electron flipping and facilitates both the $S_1 \rightarrow T_1$ (or T_m, $m > 1$) intersystem crossing and $T_1 \rightarrow S_0$ phosphorescence. It eventually produces phosphorescence with quantum yield >50% (vide supra, Table 1) and reduced phosphorescence radiative lifetime (≈0.35 µs) in vacuum deposited thin film. Particularly, the Pt···Pt (for dimer) and Pt···Pt···Pt (for trimer) interactions are mainly conveyed via their 5dz^2 orbitals (in HOMO) and resulting in a linear array of stacked structure for [Pt(pm4z)$_2$].

Table 4. The calculated wavelengths, transition probabilities, and charge transfer character of the lowest emission for the monomer of Pt(II) complex [Pt(pm4z)$_2$] in DMSO.

	State	λ [nm]	f	Main Assignments	MLCT
Dimer	$T_1 \rightarrow S_0$	497.2	0	LUMO → HOMO (51%)	17.95%
	$S_1 \rightarrow S_0$	429.5	0.1035	LUMO → HOMO (95%)	30.01%
Trimer	$T_1 \rightarrow S_0$	510.2	0	LUMO → HOMO (29%)	16.29%
	$S_1 \rightarrow S_0$	435.5	0.1966	LUMO → HOMO (49%)	30.08%

2.5. Electroluminescence

To investigate their EL properties, the following nondoped PhOLED were employed: ITO/ 4% ReO$_3$:SimCP (60 nm)/SimCP (15 nm)/emitting layer (EML) (20 nm)/PO-T2T (50 nm)/Liq (0.5 nm)/Al (100 nm), for which 3,5-di(*N*-carbazolyl)tetraphenylsilane (SimCP)[24] and ((1,3,5-triazine-2,4,6-triyl)-tris(benzene-3,1-diyl))tris(diphenylphosphine oxide) (PO-T2T)[25] were used as the hole-transporting layer (HTL) and electron-transporting

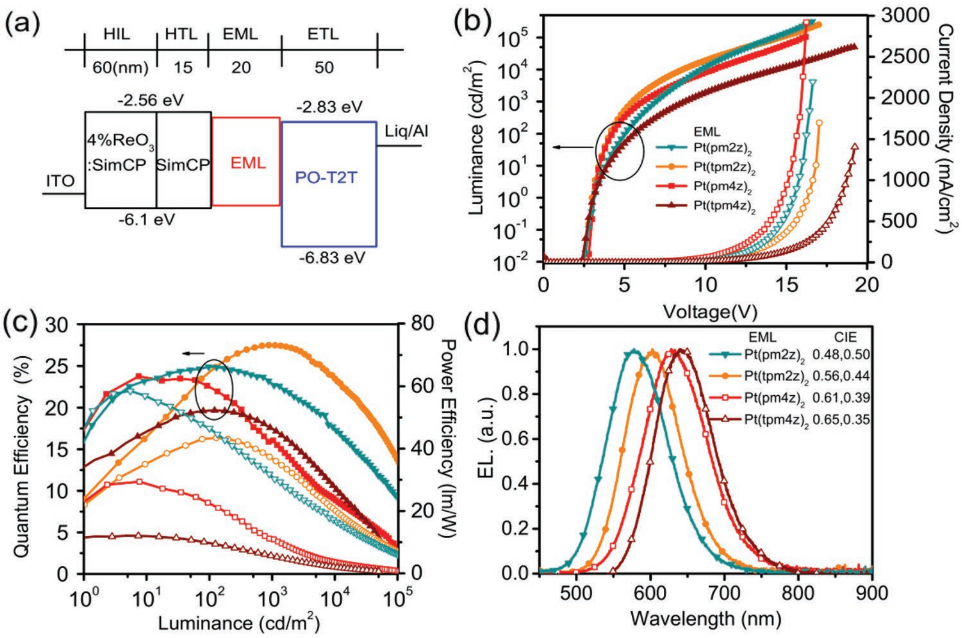

Figure 8. a) Schematic OLED structure with Pt(II) complexes as EML, b) current density–voltage–luminance (*J*–*V*–*L*) characteristics, c) EQE and power efficiencies (PE) as a function of luminance, and d) EL spectra, respectively.

layer (ETL), to achieve the optimized carrier transport. Rhenium oxides (ReO_3) in SimCP are applied as the Ohmic contact,[26] while 8-hydroxyquinolinolatolithium (Liq) and Al are used as the electron injection layer (EIL) and cathode, respectively. The device structure and the energy levels diagram are presented in **Figure 8**a. In this study, we have optimized the EML thickness and found that 20 nm of EML was the best choice for current device, which efficiently confined the exciton density at the recombination zone to maximize the performance. Figure 8b–d depicts the current density–voltage–luminance (*J*–*V*–*L*) characteristics, device efficiencies, and EL spectra, respectively. The key data are summarized in **Table 5**. All devices exhibited pure emission from phosphors and no residue emission from the adjacent layers. The emission peak maxima were located at 577, 603, 630, and 641 nm for [Pt(pm2z)$_2$], [Pt(tpm2z)$_2$], [Pt(pm4z)$_2$] and [Pt(tpm4z)$_2$] respectively, revealing spectral features similar to their thin film photoluminescence (c.f. Table 1 and Figure 2). All devices displayed a low turn-on voltage of 2.4–2.6 V. The yellow device derived from [Pt(pm2z)$_2$] achieved a maximum EQE of 24.9%, current efficiency (CE) of 74.0 cd A^{-1} and power efficiency (PE) of 58.5 lm·W^{-1} with Commission Internationale de l'éclairage (CIE) coordinates of (0.48, 0.50). By introducing t-butyl substituents in forming [Pt(tpm2z)$_2$], the orange device achieved a maximum EQE of 27.5%, CE of 64.2 cd A^{-1} and PE of 37.4 lm W^{-1} with CIE coordinates of (0.56, 0.44). In addition, the efficiency roll-off is relatively low, exhibiting EQE of 27.5% at 1000 cd m^{-2} (5.6 V), in which the EQE value was the highest among those obtained by non-doped orange devices. The red device of [Pt(pm4z)$_2$] reveals a maximum luminance (L_{max}) of 104 830 cdm^{-2} at 16.2 V (2919 mA cm^{-2}) and CIE$_{x,y}$ coordinates of (0.61, 0.39). The maximum efficiencies were measured to be 23.8%, 31.8 cd A^{-1}, and 29.4 lm W^{-1}, all of them are higher than those obtained using [Pt(tpm4z)$_2$] as emitter, c.f. 19.7%, 17.3 cd A^{-1}, and 9.4 lm W^{-1} with comparable CIE$_{x,y}$ coordinates of (0.65, 0.35), which is due to low quantum yields in neat films ($\Phi = 61\%$, see Figure S10 in the Supporting Information).

These high device performances can be attributed to the combined contribution from both high emission quantum yield of thin-film as well as the aligned horizontal orientation of the emission dipoles. It has been reported that the well aligned transition dipole moment in the plane of the substrate can increase the light out-coupling efficiency of the OLED compared to devices with randomly oriented emitting dipole moment.[27]

Table 5. EL data of OLED fabricated using respective Pt(II) metal-based emitters.

EML	$V_{on}$$^{a)}$ [V]	L_{max} [cd m^{-2}]	I_{max} [mA cm^{-2}]	EQE$_{max}$ [%]	CE$_{max}$ [cd A^{-1}]	PE$_{max}$ [lm W^{-1}]	at 10^3 nit$^{b)}$ [%, (V)]	CIE [*x*,*y*]
[Pt(pm2z)$_2$]	2.6	316400 (16.6 V)	2193	24.9	74.0	58.5	22.7% (7.0)	0.48, 0.50
[Pt(tpm2z)$_2$]	2.6	250530 (17 V)	1697	27.5	64.2	37.4	27.5% (5.6)	0.56, 0.44
[Pt(pm4z)$_2$]	2.6	104830 (16.2 V)	2919	23.8	31.8	29.4	16.0% (6.2)	0.61, 0.39
[Pt(tpm4z)$_2$]	2.4	50510 (19.2 V)	1405	19.7	17.3	9.4	17.4% (8.8)	0.65, 0.35

a)Turn-on voltage at which emission became detectable; b)The values of EQE of device at 1000 cd m^{-2}; the numbers in parentheses stand for the corresponding driving voltages.

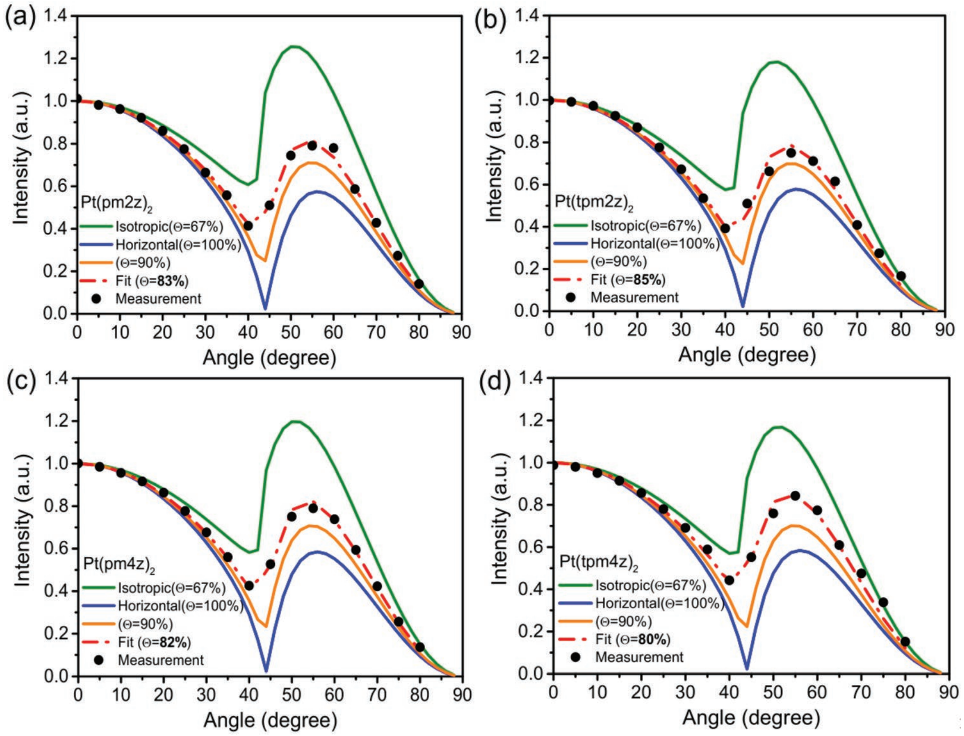

Figure 9. Angle-dependent PL intensity of *p*-polarized light at peak emission for a) [Pt(pm2z)$_2$], b) [Pt(tpm2z)$_2$], c) [Pt(pm4z)$_2$], and d) [Pt(tpm4z)$_2$] (circle) compared to simulated profiles (lines) with a different ratio of horizontal dipoles (Θ) [dashed line for fit, solid line for Θ = 1 (fully horizontal), Θ = 0. 9, and Θ = 0.67 (isotropic)].

In order to analyze the orientation of the transition dipole moment of the emitters, we measured the angular dependence of the *p*-polarized PL intensity, for which all simulated data are shown in **Figure 9** for scrutiny. Angle-dependent PL spectra at various degrees are also shown in Figure S11 in the Supporting Information. As can be seen, all horizontal dipole ratio (Θ) of those Pt(II) complexes are greater than 80%, which consistent with the observed high efficiency of the OLED devices. Hence, the high EQE of 27.5% observed for the emitter [Pt(tpm2z)$_2$] at 1000 cd·m^{-2} is attributed to both the high PLQY (Φ) of 86% and horizontal dipole ratio (Θ) of 85%.

Last but not least, we also like to point out that the recent studies on [Pt(fppz)$_2$] and analogues have already confirmed the high stability for this class of nondoped OLED devices.[28] Their robustness can be rationalized by the well organized and tightly stacked alignment of Pt(II) emitters upon deposition into EML thin film layer; hence, the fabricated OLED device is no longer subject to the commonly occurred exciton-polaron-induced aggregation degradation. The durability of such materials in OLED applications is thus very promising.

3. Conclusion

In this study, based on the strategic design and synthesis of pyrimidinyl pyrazolate Pt(II) complexes, in which the noncoordinating N-atom is placed at various positions, we are able to tune the solid-state stacking properties, and further shed light on the relationship among structure, molecular aggregation pattern and photophysical properties. In addition to the molecular identity, the stacking patterns of the titled Pt(II) complexes, as revealed by GIXD, in terms of tilting angle and stacking distances play a crucial role in manipulating the emission properties. Therefore, harnessing the stacking pattern in solid states and hence, tuning the intermolecular Pt···Pt interaction is of prime importance to promote the Pt(II) emitters in fabrication of efficient OLED. We believe that this strategy of packing molecules as a deck of poker cards can be far-reaching via ingenious ligand design in combination with the increasing power of the computational approaches to achieve exceedingly broad emission tuning from blue to near infrared region.

4. Experimental Section

General Procedures: Solvents were dried over appropriate drying agents and commercially available reagents were used without further purification. All reactions were conducted under N$_2$. Reactions were monitored by precoated TLC plates (0.20 mm with fluorescent indicator F$_{254}$). Mass spectra were obtained on a JEOL SX-102A instrument operating in electron impact (EI) or fast atom bombardment (FAB) mode. ^{1}H, ^{13}C, and ^{19}F NMR spectra were recorded on a Varian Mercury-400 or an INOVA-500 instrument. Elemental analysis was carried out with a Heraeus CHN-O-Rapid Elemental Analyzer.

General Procedures: Synthesis of [Pt(pm2z)$_2$]—A mixture of [Pt(DMSO)$_2$Cl$_2$] (0.40 g, 0.95 mmol), (pm2z)H (0.42 g, 1.98 mmol) and Na$_2$CO$_3$ (0.60 g, 5.68 mmol) in 40 mL of 2-methoxyethanol was refluxed for 12 h. The resulting precipitate was filtered and washed with deionized water, diethyl ether to afford a light yellow solid (0.47 g, 70%). Other Pt(II) complexes, namely: [Pt(tpm2z)$_2$], [Pt(pm4z)$_2$], and [Pt(tpm4z)$_2$]

were prepared under similar experimental condition in 81%, 68%, and 66%, respectively.

General Procedures: Spectral Data of [Pt(pm2z)$_2$]—^{1}H NMR (500 MHz, d$_6$-DMSO, 353 K): δ 10.41 (dd, J = 5.9, 2.1 Hz, 2H), 9.17 (dd, J = 4.9, 2.1 Hz, 2H), 7.82–7.79 (m, 2H), 7.28 (s, 2H). ^{19}F NMR (471 MHz, DMSO, 353 K): δ -59.64 (s, 6F). MS(FAB), *m/z* 621.1 [M]$^+$. Anal. Calcd. for $C_{16}H_8N_8$: C, 30.93; H, 1.30; N, 18.03. Found: 30.89; H, 1.30; N, 17.89.

General Procedures: Spectral Data of [Pt(tpm2z)$_2$]—^{1}H NMR (500 MHz, d$_7$-toluene, 353 K): δ 10.27 (d, J = 6.2 Hz, 2H), 7.15 (s, 2H), 6.39 (d, J = 6.3 Hz, 2H), 1.14 (s, 18H). ^{19}F NMR (471 MHz, d$_7$-toluene, 353 K): δ -60.74 (s, 6F). MS(FAB), *m/z* 733.2 [M]$^+$. Anal. Calcd. for $C_{24}H_{24}N_8$: C, 39.30; H, 3.30; N, 15.28. Found: 39.32; H, 3.52; N, 15.20.

General Procedures: Spectral Data of [Pt(pm4z)$_2$]—^{1}H NMR (400 MHz, d$_6$-DMSO, 353 K): δ 9.93 (d, J = 1.0 Hz, 2H), 8.86 (d, J = 5.2 Hz, 2H), 7.80 (dd, J = 5.2, 1.2 Hz, 2H), 7.16 (s, 2H). ^{19}F NMR (471 MHz, d$_6$-DMSO, 353 K): δ -59.67 (s, 6F). MS(FAB), *m/z* 621.1 [M]$^+$. Anal. Calcd. for $C_{16}H_8N_8$: C, 30.93; H, 1.30; N, 18.03. Found: 30.93; H, 1.34; N, 18.09.

General Procedures: Selected Crystal Data of [Pt(pm4z)$_2$]—$C_{16}H_8F_6N_8Pt$; M = 621.39; monoclinic; space group = $P2_1/c$; a = 10.8827(4) Å, b = 7.2509(2) Å, c = 22.2865(7)) Å, β = 101.2077(10)°; T = 150(2) K; λ(Mo K_α) = 0.71073 Å; V = 1725.08(10) Å^3; Z = 4; ρ_{calcd} = 2.393 mg·m^{-3}; F(000) = 1168; μ = 8.221 mm^{-1}; crystal size = 0.293 × 0.127 × 0.042 mm^3; 13 850 reflections, 3954 independent reflections (R_{int} = 0.0211), restraints / parameter = 24 / 293; GOF = 1.080, final R_1 [$I > 2\sigma(I)$] = 0.0265, and wR_2(all data) = 0.0499; largest diff. peak and hole = 0.884 and –0.905 e Å^{-3}.

General Procedures: Spectral Data of [Pt(tpm4z)$_2$]—^{1}H NMR (500 MHz, d$_7$-DMF, 353 K): δ 10.75 (d, J = 1.0 Hz, 2H), 8.89 (s, 2H), 7.36 (s, 2H), 1.48 (s, 18H). ^{19}F NMR (471 MHz, d$_7$-DMF, 353 K): δ -61.98 (s, 6F). MS(FAB), *m/z* 733.2 [M]$^+$. Anal. Calcd. for $C_{24}H_{24}N_8$: C, 39.30; H, 3.30; N, 15.28. Found: 39.40; H, 3.52; N, 15.33.

Grazing-Incidence X-Ray Diffraction (GIXD) Measurement: GIXD was performed at beamline 01C2 of Taiwan Light Source at National Synchrotron Radiation Research Center (NSRRC), Taiwan. All studied thin films were deposited on the Si substrate, and the GIXD data were collected using a 2D image plate (Mar345) and 12 keV X-ray beam with wavelength of 1.033 Å. The incidence angle of X-ray beam was ≈0.2° for GIXD.

Electron Density Map: Fourier reconstruction of the electron density maps were carried out using the general formula for 2D electron density as $\rho(x,y) = \sum_{hk} \sqrt{I(hk)} \exp[2\pi i(hx + ky) + i\varphi(hk)]$, where $\varphi(hk)$ are phases of structure factor (equal to 0 or π) and $I(hk)$ is intensity of Bragg peaks obtained from the GIXD patterns after background subtraction and correlation of Lorentz and polarization factors, respectively. The correct phase can be determined on the basis of physical merits of the reconstructed electron density map, aided by other information on the system coming from, e.g., other spectra or molecular simulation. The data employed for reconstruction of electron density maps are listed in Table S1a–d in the Supporting Information.

Computational Method: All calculations were performed with the Gaussian 16 program package.[29] The geometry optimization of ground states of the four Pt(II) complexes were simulated with density functional theory (DFT) at the hybrid functional PBE1PBE-D3/LANL2DZ (Pt) and PBE1PBE-D3/6-31g(d,p) (H, C, N, F) levels using DMSO as the solvent.[30] The solvent effect is based on the polarizable continuum model (PCM), which is supported implemented in the Gaussian 16 program. The optimized structures of the monomer for the four Pt(II) complexes were used to calculate the five lowest singlet ($S_0 \rightarrow S_5$) and triplet optical electronic transitions ($S_0 \rightarrow T_5$) using the time-dependent density functional theory (TDDFT) method. The optimized excited state of T_1 and S_1 for [Pt(pm4z)$_2$] dimer and trimer were also performed. For both singlet and triplet optical and emission transitions, Mulliken population analysis (MPA) was applied to obtain the electron density distribution of each atom in specific molecular orbital of the Pt(II) complexes as well as to calculate the metal-to-ligand charge transfer (MLCT) in each assignment during the singlet and triplet optical and emission transitions.

OLED Fabrications: All chemicals were purified through vacuum sublimation prior to use. The OLED were fabricated through vacuum deposition of the materials at 10^{-6} torr onto the ITO-coated glass substrates having a sheet resistance of 15 Ω sq^{-1}. Prior to use the ITO surface was cleaned ultrasonically; i.e., with acetone, methanol, and deionized water in sequence and finally with UV-ozone. The deposition rate of each organic material was ca. 1–2 Å s^{-1}. The *J–V–L* characteristics of the devices were measured simultaneously in a glove box using a Keithley 2614B source meter equipped with a calibration Si-photodiode. EL spectra were measured using a photodiode array (Ocean Optics USB2000+).

Measurement and Simulation of Angle-Dependent PL Spectra: The angular dependent *p*-polarized fluorescence intensity was measured in an attempt to analyze the transition dipole moment of emitters. The experimental setup was similar to that described in literature,[31] which composed of a motorized rotation stage, a fused silica-based half-cylindrical len, a longpass filter to stop the excitation beam, a polarizer, and a fiber-guided spectrometer (Ocean Optics USB4000) to collect the polarized emission. A continuous-wave Nd:YAG laser (355 nm, 10 kHz) was used as the excitation source which was fixed at an incident angle of 45°. The sample was deposited on top of a quartz substrate and encapsulated under N_2 atmosphere. Intensity of the *p*-polarized emission was recorded from 0° to 90° in steps of 5°. The data were analyzed using SETFOS 4.5 (Fluxim AG, Switzerland) to fit the ratio of horizontal dipoles (Θ). A completely random orientation in tris-(8-hydroxyquinoline)aluminum (Alq3) with Θ = 0.66 was employed for system calibration. As shown in Figure S12 in the Supporting Information, the refractive index n and extinction coefficient k were determined by ellipsometry (J. A. Woollam α-SE) and analyzed using Woollam CompleteEASE software.

Supporting Information

Supporting Information is available from the Wiley Online Library or from the author.

Acknowledgements

This work was supported by the funding from Ministry of Science and Technology (MOST), featured areas research program within the framework of the Higher Education Sprout Project administrated by Ministry of Education (MOE) of Taiwan, and City University of Hong Kong, Hong Kong SAR. The authors are also grateful to the National Center for High-performance Computing (NCHC) and National Synchrotron Radiation Research Center for the computer time and facilities.

Conflict of Interest

The authors declare no conflict of interest.

Keywords

aggregation, organic light emitting diodes, phosphorescent, platinum, stacking interaction

Received: January 29, 2019
Revised: April 14, 2019

---

[1] a) S. Huo, J. Carroll, D. A. K. Vezzu, *Asian J. Org. Chem.* **2015**, *4*, 1210; b) K. Li, G. S. Ming Tong, Q. Wan, G. Cheng, W.-Y. Tong, W.-H. Ang, W.-L. Kwong, C.-M. Che, *Chem. Sci.* **2016**, *7*, 1653;

c) C.-W. Lu, Y. Wang, Y. Chi, *Chem. - Eur. J.* **2016**, *22*, 17892; d) T. Strassner, *Acc. Chem. Res.* **2016**, *49*, 2680; e) C. Cebrián, M. Mauro, *Beilstein J. Org. Chem.* **2018**, *14*, 1459.

[2] a) Y. Chi, B. Tong, P.-T. Chou, *Coord. Chem. Rev.* **2014**, *281*, 1; b) Y. Chi, T.-K. Chang, P. Ganesan, P. Rajakannu, *Coord. Chem. Rev.* **2017**, *346*, 91; c) A. F. Henwood, E. Zysman-Colman, *Chem. Commun.* **2017**, *53*, 807; d) T.-Y. Li, J. Wu, Z.-G. Wu, Y.-X. Zheng, J.-L. Zuo, Y. Pan, *Coord. Chem. Rev.* **2018**, *374*, 55.

[3] J. R. Miller, *J. Chem. Soc.* **1965**, *0*, 713.

[4] a) M. Kato, K. Sasano, C. Kosuge, M. Yamazaki, S. Yano, M. Kimura, *Inorg. Chem.* **1996**, *35*, 116; b) M. Kato, C. Kosuge, K. Morii, J. S. Ahn, H. Kitagawa, T. Mitani, M. Matsushita, T. Kato, S. Yano, M. Kimura, *Inorg. Chem.* **1999**, *38*, 1638.

[5] J. Kang, X. Zhang, H. Zhou, X. Gai, T. Jia, L. Xu, J. Zhang, Y. Li, J. Ni, *Inorg. Chem.* **2016**, *55*, 10208.

[6] D. R. Klaus, M. Keene, S. Silchenko, M. Berezin, N. Gerasimchuk, *Inorg. Chem.* **2015**, *54*, 1890.

[7] M. Yoshida, M. Kato, *Coord. Chem. Rev.* **2018**, *355*, 101.

[8] a) S. C. F. Kui, S. S.-Y. Chui, C.-M. Che, N. Zhu, *J. Am. Chem. Soc.* **2006**, *128*, 8297; b) S.-Y. Chang, J.-L. Chen, Y. Chi, Y.-M. Cheng, G.-H. Lee, C.-M. Jiang, P.-T. Chou, *Inorg. Chem.* **2007**, *46*, 11202; c) A. A. Rachford, F. N. Castellano, *Inorg. Chem.* **2009**, *48*, 10865; d) C. Zhou, Y. Tian, Z. Yuan, M. Han, J. Wang, L. Zhu, M. S. Tameh, C. Huang, B. Ma, *Angew. Chem., Int. Ed.* **2015**, *54*, 9591; e) H. Leopold, M. Tenne, A. Tronnier, S. Metz, I. Münster, G. Wagenblast, T. Strassner, *Angew. Chem., Int. Ed.* **2016**, *55*, 15779; f) M. Yoshida, N. Yashiro, H. Shitama, A. Kobayashi, M. Kato, *Chem. - Eur. J.* **2016**, *22*, 491; g) K. Ohno, H. Tanuma, Y. Kusano, S. Kaizaki, A. Nagasawa, T. Fujihara, *Dalton Trans.* **2017**, *46*, 7612.

[9] a) D. Kim, J.-L. Brédas, *J. Am. Chem. Soc.* **2009**, *131*, 11371; b) J. R. Kumpfer, S. D. Taylor, W. B. Connick, S. J. Rowan, *J. Mater. Chem.* **2012**, *22*, 14196; c) X.-P. Zhang, J.-F. Mei, J.-C. Lai, C.-H. Li, X.-Z. You, *J. Mater. Chem. C* **2015**, *3*, 2350; d) K. Ohno, S. Yamaguchi, A. Nagasawa, T. Fujihara, *Dalton Trans.* **2016**, *45*, 5492; e) C.-J. Lin, Y.-H. Liu, S.-M. Peng, T. Shinmyozu, J.-S. Yang, *Inorg. Chem.* **2017**, *56*, 4978; f) L. Liu, X. Wang, N. Wang, T. Peng, S. Wang, *Angew. Chem., Int. Ed.* **2017**, *56*, 9160; g) S. Carrara, A. Aliprandi, C. F. Hogan, L. De Cola, *J. Am. Chem. Soc.* **2017**, *139*, 14605.

[10] K. Kotturi, E. Masson, *Chem. - Eur. J.* **2018**, *24*, 8670.

[11] a) M. R. R. Prabhath, J. Romanova, R. J. Curry, S. R. P. Silva, P. D. Jarowski, *Angew. Chem., Int. Ed.* **2015**, *54*, 7949; b) Y. Chi, H.-Y. Tsai, Y.-K. Chen, *J. Chin. Chem. Soc.* **2017**, *64*, 574.

[12] S.-Y. Chang, J. Kavitha, S.-W. Li, C.-S. Hsu, Y. Chi, Y.-S. Yeh, P.-T. Chou, G.-H. Lee, A. J. Carty, Y.-T. Tao, C.-H. Chien, *Inorg. Chem.* **2006**, *45*, 137.

[13] Y. Y. Noh, J. J. Kim, Y. Yoshida, K. Yase, *Adv. Mater.* **2003**, *15*, 699.

[14] Q. Wang, I. W. H. Oswald, X. Yang, G. Zhou, H. Jia, Q. Qiao, Y. Chen, J. Hoshikawa-Halbert, B. E. Gnade, *Adv. Mater.* **2014**, *26*, 8107.

[15] K.-H. Kim, J.-L. Liao, S. W. Lee, B. Sim, C.-K. Moon, G.-H. Lee, H. J. Kim, Y. Chi, J.-J. Kim, *Adv. Mater.* **2016**, *28*, 2526.

[16] K. T. Ly, R.-W. Chen-Cheng, H.-W. Lin, Y.-J. Shiau, S.-H. Liu, P.-T. Chou, C.-S. Tsao, Y.-C. Huang, Y. Chi, *Nat. Photonics* **2017**, *11*, 63.

[17] J. Mei, Y. Hong, J. W. Y. Lam, A. Qin, Y. Tang, B. Z. Tang, *Adv. Mater.* **2014**, *26*, 5429.

[18] a) P.-T. Chou, Y. Chi, *Eur. J. Inorg. Chem.* **2006**, *2006*, 3319; b) S.-Y. Chang, J. Kavitha, J.-Y. Hung, Y. Chi, Y.-M. Cheng, E. Y. Li, P.-T. Chou, G.-H. Lee, A. J. Carty, *Inorg. Chem.* **2007**, *46*, 7064.

[19] a) A. Amar, H. Meghezzi, J. Boixel, H. Le Bozec, V. Guerchais, D. Jacquemin, A. Boucekkine, *J. Phys. Chem. A* **2014**, *118*, 6278; b) P.-K. Chow, G. Cheng, G. S. M. Tong, W.-P. To, W.-L. Kwong, K.-H. Low, C.-C. Kwok, C. Ma, C.-M. Che, *Angew. Chem., Int. Ed.* **2015**, *54*, 2084; c) A. K.-W. Chan, M. Ng, Y.-C. Wong, M.-Y. Chan, W.-T. Wong, V. W.-W. Yam, *J. Am. Chem. Soc.* **2017**, *139*, 10750.

[20] a) K. M.-C. Wong, C.-K. Hui, K.-L. Yu, V. W.-W. Yam, *Coord. Chem. Rev.* **2002**, *229*, 123; b) L. Ravotto, P. Ceroni, *Coord. Chem. Rev.* **2017**, *346*, 62.

[21] a) K. M.-C. Wong, V. W.-W. Yam, *Acc. Chem. Res.* **2011**, *44*, 424; b) X. Zhang, Z. Chi, Y. Zhang, S. Liu, J. Xu, *J. Mater. Chem. C* **2013**, *1*, 3376; c) Y. Sagara, S. Yamane, M. Mitani, C. Weder, T. Kato, *Adv. Mater.* **2016**, *28*, 1073.

[22] B. Chen, X. Zeng, U. Baumeister, G. Ungar, C. Tschierske, *Science* **2005**, *307*, 96.

[23] a) C. Suryanayana, M. G. Norton, *X-Ray Diffraction A Practical Approach*, Plenum, New York **1998**; b) H. P. Klug, L. E. Alexander, *X-Ray Diffraction Procedures*, Wiley, New York **1981**.

[24] M.-F. Wu, S.-J. Yeh, C.-T. Chen, H. Murayama, T. Tsuboi, W.-S. Li, I. Chao, S.-W. Liu, J.-K. Wang, *Adv. Funct. Mater.* **2007**, *17*, 1887.

[25] W.-Y. Hung, G.-C. Fang, S.-W. Lin, S.-H. Cheng, K.-T. Wong, T.-Y. Kuo, P.-T. Chou, *Sci. Rep.* **2014**, *4*, 5161.

[26] J.-H. Lee, S.-H. Cheng, S.-J. Yoo, H. Shin, J.-H. Chang, C.-I. Wu, K.-T. Wong, J.-J. Kim, *Adv. Funct. Mater.* **2015**, *25*, 361.

[27] C. Mayr, M. Taneda, C. Adachi, W. Brütting, *Org. Electron.* **2014**, *15*, |3031.

[28] Y. Zhang, J.-L. Liao, Y. Chi, H. Aziz, *ACS Omega* **2018**, *3*, 4760.

[29] M. J. Frisch, G. W. Trucks, H. B. Schlegel, G. E. Scuseria, M. A. Robb, J. R. Cheeseman, G. Scalmani, V. Barone, B. Mennucci, G. A. Petersson, H. Nakatsuji, M. Caricato, X. Li, H. P. Hratchian, A. F. Izmaylov, J. Bloino, G. Zheng, J. L. Sonnenberg, M. Hada, M. Ehara, K. Toyota, R. Fukuda, J. Hasegawa, M. Ishida, T. Nakajima, Y. Honda, O. Kitao, H. Nakai, T. Vreven, J. A. Montgomery, J. E. Peralta, F. Ogliaro, M. Bearpark, J. J. Heyd, E. Brothers, K. N. Kudin, V. N. Staroverov, R. Kobayashi, J. Normand, K. Raghavachari, A. Rendell, J. C. Burant, S. S. Iyengar, J. Tomasi, M. Cossi, N. Rega, J. M. Millam, M. Klene, J. E. Knox, J. B. Cross, V. Bakken, C. Adamo, J. Jaramillo, R. Gomperts, R. E. Stratmann, O. Yazyev, A. J. Austin, R. Cammi, C. Pomelli, J. W. Ochterski, R. L. Martin, K. Morokuma, V. G. Zakrzewski, G. A. Voth, P. Salvador, J. J. Dannenberg, S. Dapprich, A. D. Daniels, Ö. Farkas, J. B. Foresman, J. V. Ortiz, J. Cioslowski, D. J. Fox, *Gaussian 16, Revision A03*, Gaussian Inc., Wallingford, CT **2016**.

[30] a) S. Grimme, J. Antony, S. Ehrlich, H. Krieg, *J. Chem. Phys.* **2010**, *132*, 154104; b) H. Schröder, J. Hühnert, T. Schwabe, *J. Chem. Phys.* **2017**, *146*, 044115.

[31] a) J. Frischeisen, D. Yokoyama, C. Adachi, W. Brütting, *Appl. Phys. Lett.* **2010**, *96*, 073302; b) S.-Y. Kim, W.-I. Jeong, C. Mayr, Y.-S. Park, K.-H. Kim, J.-H. Lee, C.-K. Moon, W. Brütting, J.-J. Kim, *Adv. Funct. Mater.* **2013**, *23*, 3896; c) A. Senes, S. C. J. Meskers, W. M. Dijkstra, J. J. van Franeker, S. Altazin, J. S. Wilson, R. A. J. Janssen, *J. Mater. Chem. C* **2016**, *4*, 6302.